Article:
Luus, K.A., Commane, R., Parazoo, N.C. et al. (10 more authors) (2017) Tundra photosynthesis captured by satellite-observed solar-induced chlorophyll fluorescence. Geophysical Research Letters, 44 (3). pp. 1564-1573. ISSN 0094-8276

https://doi.org/10.1002/2016GL070842

Tundra photosynthesis captured by satellite-observed solar-induced chlorophyll fluorescence

K. A. Luus[1], R. Commane[2], N. C. Parazoo[3], J. S. Benmergui[2],

S. E. Euskirchen[4], C. Frankenberg[5], J. Joiner[6], J. Lindaas[2,7], C. E. Miller[3],

W. C. Oechel[8,9], D. Zona[8,10], S. Wofsy[2], and J. C. Lin[11]

Corresponding author: K.A. Luus, (kristina.luus@gmail.com)

[1]Centre for Applied Data Analytics Research, Dublin, Ireland

[2]Harvard School of Engineering and Applied Sciences, Cambridge MA 02138, USA

[3]NASA Jet Propulsion Lab, 4800 Oak Grove Drive, Pasadena, CA 91109, USA

[4]Institute of Arctic Biology, University of Alaska Fairbanks, 902 N. Koyukuk Dr. P.O. Box 757000, Fairbanks, AK 99775, USA

[5]Environmental Science & Engineering, California Institute of Technology, CA 91125, USA

Key Points.

- Alaskan tundra has a shorter growing season and less net carbon uptake than typically estimated using satellite-derived vegetation indices.
- Comparisons against site and aircraft observations of CO_2 indicate that solar-induced fluorescence (SIF) captures tundra photosynthesis.
- SIF-driven modeling of tundra photosynthesis enables improved model accuracy, and enhanced understanding of the carbon-climate system.

Abstract. Accurately quantifying the timing and magnitude of respiration and photosynthesis by high-latitude ecosystems is important for under-

[6]NASA Goddard Space Flight Center,

Greenbelt, MD 20771, USA

[7]Department of Atmospheric Science,

Colorado State University, Fort Collins, CO,

80523

[8]San Diego State University, San Diego,

CA 92182, USA

[9]The Open University, Walton Hall,

Milton Keynes MK7 6AA, UK

[10]University of Sheffield, Sheffield, South

Yorkshire S10 2TN, UK

[11]University of Utah, Salt Lake City, UT

84112, USA

standing how a warming climate influences global carbon cycling. Data-driven estimates of photosynthesis across Arctic regions often rely on satellite-derived enhanced vegetation index (EVI); we find that satellite observations of solar-induced chlorophyll fluorescence (SIF) provide a more direct proxy for photosynthesis. We model Alaskan tundra CO_2 cycling (2012–2014) according to temperature and shortwave radiation, and alternately input EVI or SIF to prescribe the annual seasonal cycle of photosynthesis. We find that EVI-based seasonality indicates spring "green-up" to occur nine days prior to SIF-based estimates, and that SIF-based estimates agree with aircraft and tower measurements of CO_2. Adopting SIF, instead of EVI, for modeling the seasonal cycle of tundra photosynthesis can result in more accurate estimates of growing season duration and net carbon uptake by arctic vegetation.

1. Introduction

Land-atmosphere CO_2 exchange can only be continuously measured at small scales (<1 km^2), and CO_2 concentrations measured by towers and aircraft are spatially and temporally limited. Accurate, fine-resolution model estimates of net ecosystem CO_2 exchange (NEE) across large regions are therefore needed in order to gain insight into how carbon cycling by high-latitude ecosystems influences atmospheric concentrations of CO_2 and the global climate system.

Vegetation influences on rates of photosynthesis (e.g. phenology, biomass, leaf area, etc.) are typically inferred at regional scales using indices derived from satellite-observed visible and infrared reflectance, such as the normalized difference vegetation index (NDVI) and enhanced vegetation index (EVI) [*Barichivich et al.*, 2013; *Wang et al.*, 2015]. These indices are calculated as normalized ratios of visible and infrared reflectance, and rely on the tendency for vegetation chlorophyll to absorb visible (0.4–0.7 μm) radiation, and mesophyll to reflect near-infrared (0.7–1.1 μm) radiation. Larger EVI and NDVI values are indicative of denser or greener leaf cover [*Wang et al.*, 2002; *Sims et al.*, 2006], which can be interpreted as greater photosynthetic capacity.

Passive solar-induced chlorophyll fluorescence (SIF) provides a more direct proxy for photosynthesis [*Yang et al.*, 2015] independent of ancillary information or modeling steps, and can be acquired from ground- and satellite-based observations [*Frankenberg et al.*, 2014]. SIF occurs as a direct result of light absorption by the chlorophyll complex during photosynthesis [*Porcar-Castell et al.*, 2014].

Photosynthesis is therefore directly correlated with SIF [*Frankenberg et al.*, 2011a], whereas EVI is associated with the capacity of the land surface for photosynthesis. EVI is more susceptible to being confounded with non-vegetated land surface properties than SIF. Unlike SIF, EVI has been observed to remain elevated (>0) throughout most of the arctic snow season [Figure S2], and to increase during the time period over which vegetation is revealed through snowmelt. Conversely, SIF remains near zero throughout the non-growing season, and increases in response to photosynthesis [Figure 1]. Through comparisons against aircraft and tower measurements of CO_2, we show here that more realistic model estimates of tundra photosynthesis can be generated when the seasonal cycle is prescribed using SIF rather than EVI.

1.1. Overview

We present satellite-data-driven estimates of Alaskan tundra NEE (three-hourly, 0.17°×0.25°, 2012–2014) using PolarVPRM [*Luus and Lin*, 2015], a low dimensional, spatially and temporally resolved model developed according to empirical associations between site-scale meteorology and NEE. PolarVPRM-EVI has previously been applied to estimate Alaskan [*Karion et al.*, 2016] and northern Canadian [*Luus and Lin*, 2015] NEE.

We generate model estimates of Alaskan NEE, and allow the seasonal cycle of photosynthesis to alternately be driven by EVI or SIF. We then confront EVI-driven and SIF-driven estimates of Alaskan NEE (2012–2014) across tundra-dominated (>80% tundra) regions with measurements of NEE from established eddy covariance sites [Table 1; Figures 2 & S1], and observations of regional-scale CO_2 fluxes optimized from NASA's

CARVE (Carbon in the Arctic Reservoirs Vulnerability Experiment) airborne CO_2 observations [*Miller and Dinardo*, 2012].

We find that PolarVPRM-SIF is better able to capture the timing and duration of the tundra growing season (time period over which mean weekly NEE<0) than PolarVPRM-EVI. PolarVPRM-EVI overestimates growing season length, despite the application of strategies to reduce spring and fall EVI, and the inclusion of scaling factors to reduce PolarVPRM-EVI photosynthesis at the start and end of the growing season (when EVI<50% annual EVI). PolarVPRM-SIF provides improved accuracy in regional estimates of the Alaskan carbon balance [Figure S5].

2. Methods

Methods applied to: 1) observe site-scale CO_2 fluxes; 2) estimate duration of photosynthesis regionally from EVI and SIF; 3) generate regional model estimates of net ecosystem CO_2 exchange; and 4) calculate regional CO_2 fluxes from CARVE CO_2 observations, are described below.

2.1. Site-scale CO_2 observations

Measurements of net ecosystem CO_2 exchange (NEE) were obtained from established Alaskan sites using eddy covariance towers, which were used for model calibration and validation. These sites include a sparsely forested thermokarst bog in central Alaska (Bonanza Creek) [*Euskirchen et al.*, 2014], two wet sedge sites (Atqasuk & Barrow) [*Kwon et al.*, 2006; *Lipson et al.*, 2012], and a site containing wet sedge and tussock tundra (Imnavait) [*Euskirchen et al.*, 2012] [Table 1].

2.2. EVI and SIF

Moderate Resolution Imaging Spectroradiometer (MODIS) EVI observations [*Huete et al.*, 1999] were acquired from portions of the 16-day MOD13A1 dataset with good QC flags, and were smoothed using a loess filter, with spatial and temporal interpolation applied to remove missing values, and linear interpolation to ensure three-hourly estimates for all pixels. Since MODIS EVI is reported according to the maximum value observed during a given time period, it was assumed that these maximum values would correspond to the final day of observations during green-up, and to the first day of observations following the attainment of maximum annual EVI at each pixel. This approach was selected specifically to reduce EVI values in spring and autumn.

SIF was acquired across high-latitude regions using the Orbiting Carbon Observatory-2 (OCO-2) [*Frankenberg et al.*, 2011b] and Global Ozone Monitoring Experiment2 (GOME-2) [*Joiner et al.*, 2013] instruments. Retrievals from GOME-2 on MetOp-A use channel 4, with 734–758 nm wavelengths and an ≈0.5 nm spectral resolution were collected at a 1-2 day revisit time, and developed into a 0.5×0.5 degree, monthly, bias-corrected product (GOME2_F V26) by *Joiner et al.* [2013, In Press].

Retrievals from OCO-2 were taken from the Version 7 product using an algorithm described in *Frankenberg et al.* [2011b]. We used the average of Nadir soundings at 757 nm and 771 nm bands with overpass of 2:15 pm Local Time, revisit time of a few weeks, and footprint of 1.3×2.25 km^2, where the 771 nm band was multiplied by 1.35 due to its smaller signal. Soundings were aggregated to monthly averages on a $0.17^\circ \times 0.25^\circ$ grid using a minimum of 5 soundings per bin. A full-year of OCO-2 SIF estimates was generated by combining SIF observations from 2014 (Sep–Dec) and 2015 (Jan–Aug). Monthly averages

of OCO-2 SIF were generated using all available data from September 2014–August 2015, and these monthly values were repeated for all years (2012–2014).

We included GOME-2 SIF and OCO-2 SIF at a monthly resolution because our preliminary findings indicated monthly SIF values to be reliable and adequate, in agreement with *Joiner et al.* [2014]. At the regional scale, median GOME-2 SIF and OCO-2 SIF values were separately calculated for each month, and each vegetation class [Figure S4].

SIF values for each PolarVPRM pixel ($0.17° \times 0.25°$) were then calculated as the weighted mean of SIF according to component vegetation fractions, and three-hourly estimates of SIF were generated through linear interpolation of monthly values.

2.3. Estimating NEE

Estimates of NEE were generated for Alaska at a three-hourly, $0.17° \times 0.25°$ resolution using the Polar Vegetation Photosynthesis and Respiration Model (PolarVPRM) [*Luus and Lin*, 2015], a high-latitude version of VPRM [*Mahadevan et al.*, 2008]. PolarVPRM is a parametric fit to the classic hyperbolic form of the light response curve for an ecosystem of a defined vegetation type. Regional-scale estimates of NEE were acquired by calculating the weighted sum of gross ecosystem exchange (GEE,$= -1 \times$GPP) and ecosystem respiration (R) at each pixel according to its fractional vegetation cover [*Walker et al.*, 2005; *Jung et al.*, 2006; *Luus et al.*, 2013a] (see Figure S4). For a full description, evaluation and error attribution of PolarVPRM, refer to *Luus et al.* [2013b]; *Luus and Lin* [2015].

2.3.1. PolarVPRM inputs

Meteorological inputs such as soil temperature at 0-10 cm (T_{soil}), air temperature at 2 m(T_{air}), and downward shortwave radiation (PAR $= 1.98 \cdot$ SW) were provided by the

North American regional reanalysis (NARR) [*Mesinger et al.*, 2006]. Land surface conditions were estimated from MODIS snow cover area (MOD10A2) [*Hall et al.*, 2002], and land surface water index (LSWI) calculated from surface reflectance (MOD09A1) [*(MODAPS)*, 2016].

We prescribe the seasonal cycle of vegetation green-up and senescence alternately by Moderate Resolution Imaging Spectroradiometer (MODIS) EVI [*Huete et al.*, 1999], Global Ozone Monitoring Experiment2 (GOME-2) SIF [*Joiner et al.*, 2013], or Orbiting Carbon Observatory-2 (OCO-2) SIF [*Frankenberg et al.*, 2014], where SIF is normalized according to the cosine of solar zenith angle (cos(SZA)) [Figure 1].

2.3.2. PolarVPRM equations

Ecosystem respiration was calculated as a function of air (growing season) and soil (snow season) temperature depending on MODIS-derived snow cover area, using a formulation that maximizes effective capture of subnivean and growing season drivers of arctic respiration [*Luus et al.*, 2013c], including soil freeze-thaw cycles [Equation 3]. GEE was calculated according to air temperature at 2 m (T_{scale}) and photosynthetically active radiation (PAR=1.98 $\times$ shortwave radiation), such that photosynthesis (GEE) is greatest when conditions are warm and sunny. The seasonal cycle of GEE was driven alternately by MODIS EVI [Equation 1] and SIF [Equation 2].

$$\text{GEE} = \lambda \cdot \text{EVI} \cdot T_{\text{scale}} \cdot P_{\text{scale}} \cdot \frac{1}{1 + \frac{\text{PAR}}{\text{PAR}_0}} \cdot \text{PAR} \tag{1}$$

$$\text{GEE} = \lambda \cdot T_{\text{scale}} \cdot \frac{\text{SIF}}{cos(\text{SZA})} \cdot \frac{1}{1 + \frac{\text{PAR}}{\text{PAR}_0}} \cdot \text{PAR} \tag{2}$$

$$R = \begin{cases} \alpha_{\text{grow}} \cdot T_{\text{air}} + \beta_{\text{grow}} : \text{snow cover} < 50\,\% \\ \alpha_{\text{snow}} \cdot T_{\text{soil}} + \beta_{\text{snow}} : \text{snow cover} \geq 50\,\% \end{cases} . \quad (3)$$

2.3.3. PolarVPRM parameters

All parameters were calculated empirically so as to capture associations between site meteorology and eddy covariance NEE. The model parameters PAR_0 and λ [Table 2] refer to the half-saturation value of PAR and light-use efficiency at low light levels, respectively. PAR_0 was first calculated from PAR and GPP using `nls` non-linear curve fitting in R [*R Core Team*, 2013], and λ was then calculated as the slope of the linear regression of observed and modeled three-hourly GEE (with λ=1, and intercept=0) at three eddy covariance sites [Table 1]. Estimates across forested regions in interior Alaska were generated using PAR_0 and λ values in *Mahadevan et al.* [2008]. Linear regression was used to determine the slope (α) and intercept (β) of the associations between nighttime NEE (respiration) and soil/air temperature, using only values for which PAR indicated night and NEE>0.

SIF-based models used identical PAR_0 values as EVI-based models, since PAR was unchanged. However, to account for the different magnitudes of OCO-2 SIF and GOME-2 SIF relative to MODIS EVI, λ values were multiplied by a scaling factor describing the slope of EVI-based vs. SIF-based GEE at calibration eddy covariance sites. In this way, it was ensured that differences in EVI-based and SIF-based outputs would arise from inputs alone. PolarVPRM-EVI NEE additionally benefits from having corrections implemented so as to reduce the length of the modeled growing season: inclusion of scalars described in Section 2.3.4 (P_{scale}, T_{scale}), and pre-processing of EVI as described in Section 2.2.

2.3.4. PolarVPRM scalars

$$T_{\text{scale}} = \frac{(T_{\text{air}} - T_{\text{min}})(T_{\text{air}} - T_{\text{max}})}{(T_{\text{air}} - T_{\text{min}})(T_{\text{air}} - T_{\text{max}}) - (T_{\text{air}} - T_{\text{opt}})^2} \quad (4)$$

The temperature scalar [Equation 4] is calculated according to minimum (T_{min}=0∘C) and maximum (T_{max}=40∘C) temperature thresholds for photosynthesis, as well as an optimal temperature (T_{opt}). T_{opt} was set according to values in literature [*Tieszen*, 1973; *Chapin III*, 1983; *O'Sullivan et al.*, 2016] rather than being optimized in order to avoid parameter instability arising from correlations between temperature and light-use parameters [*Mahadevan et al.*, 2008] [Table 2].

In EVI-driven PolarVPRM, T_{scale} [Equation 4]ensures that GEE=0 during the snow season (when $T_{\text{air}} < 0$∘C), and reduces GPP at the start and end of the snow season, when air temperatures approach freezing. In contrast, SIF GPP estimates showed little sensitivity to T_{scale} and did not require any artificial suppression of non-growing-season photosynthesis. Final estimates of GPP by both versions of PolarVPRM include T_{scale} so as to capture mid-growing season reductions in photosynthesis due to heat stress [*O'Sullivan et al.*, 2016] in both models, and to reduce cold-season and shoulder-season GPP overestimates by PolarVPRM-EVI.

$$P_{\text{scale}} = \frac{1 + \text{LSWI}}{2} \quad (5)$$

The phenology scalar, P_{scale}, is prescribed in the EVI version of VPRM and PolarVPRM to reduce photosynthesis when EVI is at $< 50\%$ of maximum annual pixel-specific EVI, so as to reduce overestimates of photosynthesis in spring and fall [Equation 5]. This was applied in the EVI version of PolarVPRM to reduce errors arising from elevated (>0) EVI before and after the growing season, but was not needed in the SIF version of

PolarVPRM. In short, the two scalar terms, T_{scale} and P_{scale}, both reduce overestimates of GPP by PolarVPRM-EVI, especially at the start and end of the growing season.

2.4. Regional-scale CO_2 observations

CO_2 concentrations were measured during Carbon in Arctic Reservoirs Vulnerability Experiment (CARVE) flight campaigns, which were conducted over Alaska throughout the 2012-2014 growing seasons. The NASA C-23B (N430NA) aircraft was based in Fairbanks, Alaska, USA, and flights sampled the region between 55°–72°N and 165°–138°W. CO_2, CH_4 and CO were measured using two independent cavity ringdown spectrometers: one operated wet (G1301-m in 2012 and G2401-m from 2013 onward) [*Karion et al.*, 2013] and one dry (G2401-m) [*Chang et al.*, 2014]. Each analyzer was calibrated throughout the flights, with gap-filling to ensure a continuous 5 s time series.

Airborne CO_2 concentrations (ppm) were modeled to gain insight into the magnitudes and locations of CO_2 fluxes (μmol m^{-2} s^{-1}) giving rise to observed CO_2 concentrations. First, modeled column CO_2 concentrations were calculated for altitude profiles within each flight using pWRF-STILT (polar variant of Weather Forecasting and Research - Stochastic Time Inverted Lagrangian Transport model) [*Henderson et al.*, 2015; *Lin et al.*, 2003] mapping of land surface influences on mean three-hourly CO_2 concentrations. These results are provided on a 0.5°×0.5° grid that represents the response of each receptor to a unit emission of CO_2 at each grid square (in $\frac{\mu\text{mol}}{mol}/\frac{\mu\text{mol}}{\text{m}^2\text{s}}$). The column integral represents the mass loading of regional emissions on the atmosphere from the surface to the top of the mixed layer. The column enhancement of CO_2 mole fractions combines all fluxes to give an integrated signal used in the column analysis. Episodic or point sources of CO_2 will have little influence on this integrated signal.

Alaskan NEE was calculated from these CARVE CO_2 datasets. Mean monthly additive fluxes (δF, in $\frac{\mu mol}{m^2 s}$) were calculated as the difference between the integrated column enhancement of the observed and modeled CO_2 for each profile, and were calculated separately using PolarVPRM-EVI and PolarVPRM-SIF. CARVE-constrained estimates of NEE were then generated by adding δF to the mean spatially averaged NEE from PolarVPRM-EVI and PolarVPRM-SIF.

CARVE NEE fluxes are a result of mass balance considerations based upon tracer variations in the atmospheric planetary boundary layer, which is the most direct means we have possible to observe and quantify regional carbon fluxes. The mean of the 273 CARVE column profiles used for this approach is shown in Figure 3, along with the standard deviation of the additive flux from each of these profiles, to indicate quantitatively the uncertainty of CARVE fluxes. For additional details regarding the approach used to examine CARVE CO_2 observations, please refer to *Henderson et al.* [2015].

3. Results

3.1. Site-scale

We confronted both PolarVPRM-EVI and PolarVPRM-SIF NEE with site-scale observations of NEE collected at four established Alaskan eddy covariance sites (2012–2014) [Table 1]. PolarVPRM-EVI NEE overestimated the timing and magnitude of late winter photosynthesis at bog, sedge and tussock tundra sites. Unlike SIF, EVI increased during late winter snowmelt [Figure 1], and remained elevated throughout the late snow season [Figure S2]. Overall, growing season onset was better captured using PolarVPRM-SIF than PolarVPRM-EVI at tundra sites [Figure 2].

If the carbon uptake period is estimated from EVI, the start of the tundra growing season is therefore assumed to occur earlier than observed at the site-scale. Since solar radiation is used to estimate photosynthesis, the coincident timing of the solar maximum, and snowmelt-induced increases in EVI conspire to result in large overestimates of spring photosynthesis. Conversely, applying a SIF-based approach enables model estimates to capture the timing of peak photosynthesis [Figure 2].

3.2. Regional

A comparison of NEE modeled using SIF and EVI to CARVE-optimized NEE revealed a tendency for spring photosynthetic uptake to be overestimated when the seasonal cycle was prescribed using EVI [Figure 3]. Evaluation of daily mean model NEE against daily mean CARVE NEE indicated that the SIF-based model had a root-mean-square error (RMSE) of 0.387 μmol m^{-2} s^{-1}, whereas the EVI-based model had an RMSE of 0.579 μmol m^{-2} s^{-1}. CARVE-optimized NEE indicated that the growing season (when weekly NEE<0) began on days 160, 167 and 161, in 2012, 2013 and 2014, respectively. Relative to CARVE data, EVI-based estimates of NEE indicated the growing season to begin 9, 20 and 16 days too early, whereas the SIF-based approach underestimated these dates by only 1, 9 and 8 days. This corresponds to biases of 15 days by PolarVPRM-EVI and 6 days by PolarVPRM-SIF.

GOME-2 SIF more accurately captures the seasonal cycle of tundra photosynthesis than MODIS EVI. Prescribing a seasonal cycle of photosynthesis using GOME-2 SIF rather than MODIS EVI resulted in improved agreement between modeled and observed NEE across Alaska's tundra-dominated regions. Overestimates of tundra photosynthesis by EVI-driven models result in diminished accuracy in estimates of Alaska's carbon cy-

cle [Figure S6], whereas SIF-driven estimates show reasonable agreement with CARVE observations across Alaska [Figure S5].

4. Discussion

4.1. SIF captures spring photosynthetic onset better than EVI

Whereas EVI represents the presence, quantity or health of aboveground vegetation [*Wang et al.*, 2002; *Sims et al.*, 2006], from which photosynthetic capacity can be inferred, SIF occurs as a direct result of light absorption by the chlorophyll complex [*Yang et al.*, 2015; *Frankenberg et al.*, 2014; *Parazoo et al.*, 2013]. SIF is therefore more likely than EVI to capture the lag between initial spring snowmelt, start of growing season (NEE<0), and onset of high rates of canopy photosynthesis [*Joiner et al.*, 2014].

In snow-dominated regions, EVI can remain elevated (>0) throughout most of the snow season if canopy height exceeds snow depth, or if influenced by non-vegetation land surface properties [Figure S2]. In late winter, EVI rises quickly from a non-zero base value in response to the appearance of senescent vegetation revealed through snowmelt, and confounding changes over time in non-chlorophyll containing surface properties, rather than due to leaf out or photosynthetic onset [*Fontana et al.*, 2008; *Jin and Eklundh*, 2014]. The combination of these errors in estimating the seasonal cycle of photosynthesis using EVI would be difficult to correct fully for across large, heterogeneous and cloudy region such as Alaska.

EVI-driven models can estimate photosynthesis to occur throughout the portion of the late snow season and early growing season where warm (> 0°C) and sunny conditions prevail. The timing of snowmelt and photosynthesis may initially coincide when evergreen arctic vegetation rapidly begins to photosynthesize during initial snowmelt while

air temperatures and subnivean CO_2 concentrations are high [*Starr and Oberbauer*, 2003]. However, productivity has been observed to stall following snowmelt, and the rate of net CO_2 efflux has been observed to increase slightly when exposed to freeze-thaw cycles [*Larsen et al.*, 2007]. Without the insulating effect of a dry snowpack, vegetation is likely to be more vulnerable to cold air temperatures during and following snowmelt, which can cause damage and disproportionately hinder green-up, leaf-out and photosynthetic onset [*Bokhorst et al.*, 2009]. Relying on EVI for modeling Arctic NEE can therefore result in overestimates of photosynthetic rates throughout the late snow season and early growing season.

4.2. Tundra NEE is better captured by SIF than EVI

SIF reliably captures the seasonal cycle of tundra photosynthesis, which is consistent with previous studies of non-Arctic ecosystems (i.e. savannas [*Pérez-Priego et al.*, 2015], rainforests [*Lee et al.*, 2013], forests [*Walther et al.*, 2015], crops [*Guanter et al.*, 2014]). Establishing the utility of SIF for tundra regions provides further motivation for widespread application of a SIF-based approach to global carbon cycle modeling.

Using SIF, rather than EVI, to estimate tundra NEE enables closer agreement between modeled and observed NEE due mainly to differences in timing of growing season onset, and the tendency for SIF to remain near 0 throughout the non-growing season. Similar seasonal patterns in APAR relative to SIF have been observed in boreal forests [*Joiner et al.*, 2013], and we find similar patterns in Alaskan MODIS GPP [*Running and Zhao*, 2015] [Figure S6]. Additionally, whereas PolarVPRM-EVI requires scalar terms to reduce shoulder season photosynthesis and suppress cold season photosynthesis, SIF provides

more direct estimates of tundra's seasonal cycle, and so can be included parsimoniously in models.

Arctic warming caused by climate change can both enable more carbon uptake by high-latitude vegetation due to a lengthening growing season [*Goetz et al.*, 2005; *Groendahl et al.*, 2007], and increase rates of carbon release from thawing permafrost [*Schuur et al.*, 2008]. Accurately monitoring the Arctic carbon balance is important due to the immense quantity ($\approx$ 1700 Gt) of soil organic carbon [*Tarnocai et al.*, 2009] underlying Arctic regions, and positive feedbacks between climate warming and greenhouse gas emissions from permafrost [*Schuur et al.*, 2015]. Accurately characterizing net carbon uptake by tundra ecosystems at the regional scale, and monitoring changes over time in growing season onset and length, are therefore critically important.

4.3. SIF-based modeling of tundra NEE

Satellite-data-driven estimates of tundra photosynthesis can be calculated empirically from meteorological observations and SIF, according to site-scale associations between NEE and meteorology. Accurate model estimates of regional-scale carbon cycling rely on an appropriate model formulation, parameter fitting, selection of satellite indices, and processing of satellite inputs to the model.

In light of the similarity in estimates of tundra NEE generated from OCO-2 SIF and GOME-2 SIF, future work may focus on examining the potential to create a blended product that exploits GOME-2's longer data record and complete spatial coverage, and OCO-2's finer spatial resolution. Further reductions in uncertainty regarding global photosynthesis will likely also result from combining SIF observations from OCO-2 and GOME-2 with SIF retrieved by the TROPOspheric Monitoring Instrument (TROPOMI).

TROPOMI will have a wide swath, high signal-to-noise ratio, fine spatial resolution in global composites (0.1 °), and large number of clear-sky observations over land per day relative to existing products [*Guanter et al.*, 2015].

The results presented here also suggest strategies for improving the accuracy of process-based estimates of high-latitude CO_2 cycling. Regional estimates of CO_2 concentrations over time by thirteen established process-based models were recently evaluated relative to atmospheric observations of CO_2 through the International Land Model Benchmarking Project (ILAMB) [*Hoffman et al.*, 2015]. Findings indicated systematic springtime overestimates of net carbon uptake by vegetation across high-latitude Northern regions (50–70° N), due in part to an overly early start to the growing season. Photosynthesis in these process-based models was simulated using strategies resembling both SIF-based [*Ball et al.*, 1987] and EVI-based [*Roberts et al.*, 2004] approaches. Overestimates of spring photosynthetic uptake in these models may occur when deciduous growth of photosynthetic tissues or evergreen recovery from cold hardening are simulated to occur faster than they actually do [*Bergh et al.*, 1998]. Improved accuracy in process-based modeling of Arctic carbon cycling could therefore potentially be attained by simulating lags between green-up and growing season onset using tundra-specific stress factors relating to vegetation photosynthetic capacity.

5. Conclusions

SIF captures the timing of spring green-up, and seasonal cycle of photosynthesis across Alaskan tundra. EVI indicates tundra growing season onset to occur an average of nine days sooner than SIF. EVI-driven estimates of arctic NEE likely estimate growing season onset to occur too soon, and may overestimate growing season duration [Figure S6].

Alaskan tundra carbon cycling can be accurately modeled using an empirical, data-driven approach integrating satellite observations of SIF, temperature and shortwave radiation. Prescribing the seasonal cycle of photosynthesis according to SIF enables accurate modeling of tundra NEE relative to tower and aircraft CO_2 measurements (RMSE=0.39 μmol m^{-2} s^{-1}). Alaskan carbon budget estimates are biased towards too much uptake if growing season length is prescribed by EVI instead of SIF [Figure S5].

Using an SIF-based approach to estimate tundra canopy photosynthesis therefore provides improved understanding of the extent to which high-latitude regions are taking up and releasing carbon, and how this is changing over time. SIF-driven modeling of tundra photosynthesis enables improved constraints on the tundra carbon cycle, and enhanced understanding of feedbacks between Arctic carbon cycling and climate change.

6. Acknowledgements

The authors wish to acknowledge contributions from the the OCO-2 and GOME-2 teams. Funding from NSERC through a Postdoctoral Fellowship (KAL) is gratefully acknowledged. Some of the research described in this paper was performed for the Carbon in Arctic Reservoirs Vulnerability Experiment (CARVE), an Earth Ventures (EV-1) investigation, under contract with NASA. A portion of the research described in this paper was performed at the Jet Propulsion Laboratory, California Institute of Technology, under contract with the National Aeronautics and Space Administration. Data from Imnavait, Alaska were provided by E. Euskirchen, C. Edgar, and M. S. Bret-Harte and collected through a grant from the National Science Foundation Collaborative Research on Carbon, Water, and Energy Balance of the Arctic Landscape at Flagship Observatories in Alaska and Siberia. Eddy covariance and meteorological observations from Ivotuk, Bar-

row and Atqasuk were generously provided by W. Oechel and his group. Funding and support were provided by the U.S. Department of Energy (National Institute for Climatic Change Research (NICCR), TES program (DESC005160)), and the National Science Foundation (Arctic System Sciences, the Land-Atmosphere- Ice Interactions (LAII) program (OPP-9732109), the Joint Program on Terrestrial Ecology and Global Change Notice 97-02 (TECO), program DEB 97-3004, Environmental Research and Education (OPP-0421588 BE/CBC)). We also wish to thank Adrian Rocha for providing site-scale observations of EVI. NCEP Reanalysis data provided by the NOAA/OAR/ESRL PSD, Boulder, Colorado, USA, from their Web site at http://www.esrl.noaa.gov/psd/ The MODIS MOD13A1, MOD10A2 and MOD09A1 data products were retrieved from the online Data Pool, courtesy of the NASA Land Processes Distributed Active Archive Center (LP DAAC), USGS/Earth Resources Observation and Science (EROS) Center, Sioux Falls, South Dakota, https://lpdaac.usgs.gov/data_access/data_pool. MOD17A2 GPP was provided by the Numerical Terradynamic Simulation Group (NTSG) at the University of Montana. We wish to thank the Oak Ridge National Lab for hosting open access to all Alaskan PolarVPRM outputs presented here, which can be downloaded from *Luus and Lin* [2016].

References

Ball, J. T., I. E. Woodrow, and J. A. Berry (1987), A model predicting stomatal conductance and its contribution to the control of photosynthesis under different environmental conditions, in *Progress in photosynthesis research*, pp. 221–224, Springer.

Barichivich, J., K. R. Briffa, R. B. Myneni, T. J. Osborn, T. M. Melvin, P. Ciais, S. Piao, and C. Tucker (2013), Large-scale variations in the vegetation growing season and annual cycle of atmospheric co2 at high northern latitudes from 1950 to 2011, *Global change biology*, *19*(10), 3167–3183.

Bergh, J., R. E. McMurtrie, and S. Linder (1998), Climatic factors controlling the productivity of norway spruce: a model-based analysis, *Forest ecology and management*, *110*(1), 127–139.

Bokhorst, S. F., J. W. Bjerke, H. Tømmervik, T. V. Callaghan, and G. K. Phoenix (2009), Winter warming events damage sub-Arctic vegetation: consistent evidence from an experimental manipulation and a natural event, *Journal of Ecology*, *97*(6), 1408–1415.

Chang, R. Y.-W., C. E. Miller, S. J. Dinardo, A. Karion, C. Sweeney, B. C. Daube, J. M. Henderson, M. E. Mountain, J. Eluszkiewicz, J. B. Miller, et al. (2014), Methane emissions from Alaska in 2012 from CARVE airborne observations, *Proceedings of the National Academy of Sciences*, *111*(47), 16,694–16,699.

Chapin III, F. (1983), Direct and indirect effects of temperature on arctic plants, *Polar Biology*, *2*(1), 47–52.

Euskirchen, E., M. S. Bret-Harte, G. Scott, C. Edgar, and G. R. Shaver (2012), Seasonal patterns of carbon dioxide and water fluxes in three representative tundra ecosystems in northern Alaska, *Ecosphere*, *3*(1), art4.

Euskirchen, E., C. Edgar, M. Turetsky, M. Waldrop, and J. Harden (2014), Differential response of carbon fluxes to climate in three peatland ecosystems that vary in the presence and stability of permafrost, *Journal of Geophysical Research: Biogeosciences*, *119*(8), 1576–1595.

Fontana, F., C. Rixen, T. Jonas, G. Aberegg, and S. Wunderle (2008), Alpine grassland phenology as seen in AVHRR, VEGETATION, and MODIS NDVI time series-a comparison with in situ measurements, *Sensors*, *8*(4), 2833–2853.

Frankenberg, C., J. B. Fisher, J. Worden, G. Badgley, S. S. Saatchi, J.-E. Lee, G. C. Toon, A. Butz, M. Jung, A. Kuze, et al. (2011a), New global observations of the terrestrial carbon cycle from gosat: Patterns of plant fluorescence with gross primary productivity, *Geophysical Research Letters*, *38*(17).

Frankenberg, C., A. Butz, and G. C. Toon (2011b), Disentangling chlorophyll fluorescence from atmospheric scattering effects in O2 A-band spectra of reflected sun-light, *Geophysical Research Letters*, *38*(3), doi:10.1029/2010GL045896, l03801.

Frankenberg, C., C. O'Dell, J. Berry, L. Guanter, J. Joiner, P. Köhler, R. Pollock, and T. E. Taylor (2014), Prospects for chlorophyll fluorescence remote sensing from the Orbiting Carbon Observatory-2, *Remote Sensing of Environment*, *147*, 1–12.

Goetz, S. J., A. G. Bunn, G. J. Fiske, and R. Houghton (2005), Satellite-observed photosynthetic trends across boreal North America associated with climate and fire disturbance, *Proceedings of the National Academy of Sciences of the United States of America*, *102*(38), 13,521–13,525.

Groendahl, L., T. Friborg, and H. Sogaard (2007), Temperature and snow-melt controls on interannual variability in carbon exchange in the high arctic, *Theoretical and Applied Climatology*, *88*(1-2), 111–125.

Guanter, L., Y. Zhang, M. Jung, J. Joiner, M. Voigt, J. A. Berry, C. Frankenberg, A. R. Huete, P. Zarco-Tejada, J.-E. Lee, et al. (2014), Global and time-resolved monitoring of crop photosynthesis with chlorophyll fluorescence, *Proceedings of the National Academy*

401 *of Sciences*, *111*(14), E1327–E1333.

402 Guanter, L., I. Aben, P. Tol, J. Krijger, A. Hollstein, P. Köhler, A. Damm, J. Joiner,
403 C. Frankenberg, and J. Landgraf (2015), Potential of the TROPOspheric Monitoring
404 Instrument (TROPOMI) onboard the Sentinel-5 Precursor for the monitoring of terres-
405 trial chlorophyll fluorescence, *Atmospheric Measurement Techniques*, *8*, 1337–1352.

406 Hall, D. K., G. A. Riggs, V. V. Salomonson, N. E. DiGirolamo, and K. J. Bayr (2002),
407 MODIS snow-cover products, *Remote sensing of Environment*, *83*(1), 181–194.

408 Henderson, J., J. Eluszkiewicz, M. Mountain, T. Nehrkorn, R. Chang, A. Karion, J. Miller,
409 C. Sweeney, N. Steiner, S. Wofsy, et al. (2015), Atmospheric transport simulations in
410 support of the Carbon in Arctic Reservoirs Vulnerability Experiment (CARVE), *Atmos*
411 *Chem Phys*, *15*(8), 4093–4116.

412 Hoffman, F. M., W. J. Riley, J. T. Randerson, S. M. Elliott, G. Keppel-Aleks, C. D.
413 Koven, D. M. Lawrence, U. Mishra, J. K. Moore, and X. Yang (2015), Biogeochemistry–
414 climate feedbacks: Quantifying feedbacks and uncertainties of biogeochemical processes
415 in Earth System Models.

416 Huete, A., C. Justice, and W. Van Leeuwen (1999), MODIS vegetation index (MOD13),
417 *Algorithm theoretical basis document*, *3*, 213.

418 Jin, H., and L. Eklundh (2014), A physically based vegetation index for improved moni-
419 toring of plant phenology, *Remote Sensing of Environment*, *152*, 512–525.

420 Joiner, J., L. Guanter, R. Lindstrot, M. Voigt, A. Vasilkov, E. Middleton, K. Huemm-
421 rich, Y. Yoshida, and C. Frankenberg (2013), Global monitoring of terrestrial chloro-
422 phyll fluorescence from moderate-spectral-resolution near-infrared satellite measure-
423 ments: methodology, simulations, and application to GOME-2, *Atmospheric Measure-*

ment Techniques, *6*(10), 2803–2823.

Joiner, J., Y. Yoshida, A. Vasilkov, K. Schaefer, M. Jung, L. Guanter, Y. Zhang, S. Garrity, E. Middleton, K. Huemmrich, et al. (2014), The seasonal cycle of satellite chlorophyll fluorescence observations and its relationship to vegetation phenology and ecosystem atmosphere carbon exchange, *Remote Sensing of Environment*, *152*, 375–391.

Joiner, J., Y. Yoshida, L. Guanter, and E. M. Middleton (In Press), New methods for retrieval of chlorophyll red fluorescence from hyper-spectral satellite instruments: simulations and application to GOME-2 and SCIAMACHY, *Atmospheric Measurement Techniques Discussions*, pp. doi:10.5194/amt–2015–387.

Jung, M., K. Henkel, M. Herold, and G. Churkina (2006), Exploiting synergies of global land cover products for carbon cycle modeling, *Remote Sensing of Environment*, *101*(4), 534–553.

Karion, A., C. Sweeney, S. Wolter, T. Newberger, H. Chen, A. Andrews, J. Kofler, D. Neff, and P. Tans (2013), Long-term greenhouse gas measurements from aircraft, *Atmospheric Measurement Techniques*, *6*(3), 511–526.

Karion, A., C. Sweeney, J. B. Miller, A. E. Andrews, R. Commane, S. Dinardo, J. M. Henderson, J. Lindaas, J. C. Lin, K. A. Luus, T. Newberger, P. Tans, S. C. Wofsy, S. Wolter, and C. E. Miller (2016), Investigating Alaskan methane and carbon dioxide fluxes using measurements from the CARVE tower, *Atmospheric Chemistry and Physics*, *16*(8), 5383–5398, doi:10.5194/acp-16-5383-2016.

Kwon, H.-J., W. C. Oechel, R. C. Zulueta, and S. J. Hastings (2006), Effects of climate variability on carbon sequestration among adjacent wet sedge tundra and moist tussock tundra ecosystems, *Journal of Geophysical Research: Biogeosciences*, *111*(G3).

Larsen, K. S., A. Ibrom, S. Jonasson, A. Michelsen, and C. Beier (2007), Significance of cold-season respiration and photosynthesis in a subarctic heath ecosystem in Northern Sweden, *Global Change Biology*, *13*(7), 1498–1508.

Lee, J.-E., C. Frankenberg, C. van der Tol, J. A. Berry, L. Guanter, C. K. Boyce, J. B. Fisher, E. Morrow, J. R. Worden, S. Asefi, et al. (2013), Forest productivity and water stress in Amazonia: observations from GOSAT chlorophyll fluorescence, *Proceedings of the Royal Society of London B: Biological Sciences*, *280*(1761), 20130,171.

Lin, J., C. Gerbig, S. Wofsy, A. Andrews, B. Daube, K. Davis, and C. Grainger (2003), A near-field tool for simulating the upstream influence of atmospheric observations: The stochastic time-inverted lagrangian transport (STILT) model, *Journal of Geophysical Research: Atmospheres (1984–2012)*, *108*(D16).

Lipson, D. A., D. Zona, T. K. Raab, F. Bozzolo, M. Mauritz, and W. C. Oechel (2012), Water table height and microtopography control biogeochemical cycling in an arctic coastal tundra ecosystem, *Biogeosciences*, *9*, 577–591.

Luus, K., and J. Lin (2015), The Polar Vegetation Photosynthesis and Respiration Model (PolarVPRM): a parsimonious, satellite data-driven model of high-latitude co_2 exchange, *Geoscientific Model Development*, *8*(2), 979–1027.

Luus, K., and J. Lin (2016), CARVE Modeled Gross Ecosystem CO2 Exchange and Respiration, Alaska, 2012-2014, http://dx.doi.org/10.3334/ORNLDAAC/1314.

Luus, K., Y. Gel, J. Lin, R. Kelly, and C. Duguay (2013a), Pan-Arctic linkages between snow accumulation and growing-season air temperature, soil moisture and vegetation, *Biogeosciences*, *10*, 7575–7597.

Luus, K., R. Kelly, J. Lin, E. Humphreys, P. Lafleur, and W. Oechel (2013b), Modeling the influence of snow cover on low Arctic net ecosystem exchange, *Environmental Research Letters*, *8*(3), 035,045.

Luus, K. A., J. C. Lin, R. E. Kelly, and C. R. Duguay (2013c), Subnivean Arctic and sub-Arctic net ecosystem exchange (NEE): towards representing snow season processes in models of Nee using cryospheric remote sensing, *Progress in Physical Geography*, *37*(4), 484–515.

Mahadevan, P., S. C. Wofsy, D. M. Matross, X. Xiao, A. L. Dunn, J. C. Lin, C. Gerbig, J. W. Munger, V. Y. Chow, and E. W. Gottlieb (2008), A satellite-based biosphere parameterization for net ecosystem CO2 exchange: Vegetation Photosynthesis and Respiration Model (VPRM), *Global Biogeochemical Cycles*, *22*(2).

Mesinger, F., G. DiMego, E. Kalnay, K. Mitchell, P. C. Shafran, W. Ebisuzaki, D. Jovic, J. Woollen, E. Rogers, E. H. Berbery, et al. (2006), North American regional reanalysis, *Bulletin of the American Meteorological Society*, *87*(3), 343–360.

Miller, C. E., and S. J. Dinardo (2012), CARVE: The Carbon in arctic reservoirs vulnerability experiment, in *Aerospace conference, 2012 IEEE*, pp. 1–17, IEEE.

(MODAPS), M. L. S. T. A. P. S. (2016), MODIS/Terra Atmospherically Corrected Surface Reflectance 5Min L2 Swath 250m 500m 1km, http://dx.doi.org/10.5067/MODIS/MOD09.NRT.006.

O'Sullivan, O. S., M. A. Heskel, P. B. Reich, M. G. Tjoelker, K. L. K. Weerasinghe, A. Penillard, L. Zhu, J. J. Egerton, K. J. Bloomfield, D. Creek, N. H. A. Bahar, K. L. Griffin, V. Hurry, P. Meir, M. H. Turnbull, and O. K. Atkin (2016), Thermal limits of leaf metabolism across biomes, *Global Change Biology*, pp. n/a–n/a, doi:10.1111/gcb.13477.

Parazoo, N. C., K. Bowman, C. Frankenberg, J.-E. Lee, J. B. Fisher, J. Worden, D. Jones, J. Berry, G. J. Collatz, I. T. Baker, et al. (2013), Interpreting seasonal changes in the carbon balance of southern Amazonia using measurements of XCO2 and chlorophyll fluorescence from GOSAT, *Geophysical Research Letters*, *40*(11), 2829–2833.

Pérez-Priego, O., J.-H. Guan, M. Rossini, F. Fava, T. Wutzler, G. Moreno, N. Carvalhais, A. Carrara, O. Kolle, T. Julitta, et al. (2015), Sun-induced chlorophyll fluorescence and photochemical reflectance index improve remote-sensing gross primary production estimates under varying nutrient availability in a typical Mediterranean savanna ecosystem, *Biogeosciences*, *12*, 6351–6367.

Porcar-Castell, A., E. Tyystjärvi, J. Atherton, C. van der Tol, J. Flexas, E. E. Pfündel, J. Moreno, C. Frankenberg, and J. A. Berry (2014), Linking chlorophyll a fluorescence to photosynthesis for remote sensing applications: mechanisms and challenges, *Journal of Experimental Botany*, p. eru191.

R Core Team (2013), *R: A Language and Environment for Statistical Computing*, R Foundation for Statistical Computing, Vienna, Austria.

Roberts, D. A., S. L. Ustin, S. Ogunjemiyo, J. Greenberg, S. Z. Dobrowski, J. Chen, and T. M. Hinckley (2004), Spectral and structural measures of northwest forest vegetation at leaf to landscape scales, *Ecosystems*, *7*(5), 545–562.

Running, S. W., and M. Zhao (2015), Daily GPP and Annual NPP (MOD17A2/A3) products NASA Earth Observing System MODIS land algorithm.

Schuur, E., A. McGuire, C. Schädel, G. Grosse, J. Harden, D. Hayes, G. Hugelius, C. Koven, P. Kuhry, D. Lawrence, et al. (2015), Climate change and the permafrost carbon feedback, *Nature*, *520*(7546), 171–179.

Schuur, E. A., J. Bockheim, J. G. Canadell, E. Euskirchen, C. B. Field, S. V. Goryachkin, S. Hagemann, P. Kuhry, P. M. Lafleur, H. Lee, et al. (2008), Vulnerability of permafrost carbon to climate change: implications for the global carbon cycle, *BioScience*, *58*(8), 701–714.

Sims, D. A., A. F. Rahman, V. D. Cordova, B. Z. El-Masri, D. D. Baldocchi, L. B. Flanagan, A. H. Goldstein, D. Y. Hollinger, L. Misson, R. K. Monson, et al. (2006), On the use of MODIS EVI to assess gross primary productivity of North American ecosystems, *Journal of Geophysical Research: Biogeosciences (2005–2012)*, *111*(G4).

Starr, G., and S. F. Oberbauer (2003), Photosynthesis of arctic evergreens under snow: implications for tundra ecosystem carbon balance, *Ecology*, *84*(6), 1415–1420.

Tarnocai, C., J. Canadell, E. Schuur, P. Kuhry, G. Mazhitova, and S. Zimov (2009), Soil organic carbon pools in the northern circumpolar permafrost region, *Global biogeochemical cycles*, *23*(2).

Tieszen, L. L. (1973), Photosynthesis and respiration in arctic tundra grasses: field light intensity and temperature responses, *Arctic and Alpine Research*, pp. 239–251.

Walker, D. A., M. K. Raynolds, F. J. Daniëls, E. Einarsson, A. Elvebakk, W. A. Gould, A. E. Katenin, S. S. Kholod, C. J. Markon, E. S. Melnikov, et al. (2005), The circumpolar arctic vegetation map, *Journal of Vegetation Science*, *16*(3), 267–282.

Walther, S., M. Voigt, T. Thum, A. Gonsamo, Y. Zhang, P. Koehler, M. Jung, A. Varlagin, and L. Guanter (2015), Satellite chlorophyll fluorescence measurements reveal large-scale decoupling of photosynthesis and greenness dynamics in boreal evergreen forests, *Global change biology*.

Wang, X., S. Piao, X. Xu, P. Ciais, N. MacBean, R. B. Myneni, and L. Li (2015), Has the advancing onset of spring vegetation green-up slowed down or changed abruptly over the last three decades?, *Global Ecology and Biogeography*, *24*(6), 621–631.

Wang, Z., C. Liu, and A. Huete (2002), From AVHRR-NDVI to MODIS-EVI: advances in vegetation index research, *Acta ecologica sinica*, *23*(5), 979–987.

Yang, X., J. Tang, J. F. Mustard, J.-E. Lee, M. Rossini, J. Joiner, J. W. Munger, A. Kornfeld, and A. D. Richardson (2015), Solar-induced chlorophyll fluorescence that correlates with canopy photosynthesis on diurnal and seasonal scales in a temperate deciduous forest, *Geophysical Research Letters*, *42*(8), 2977–2987.

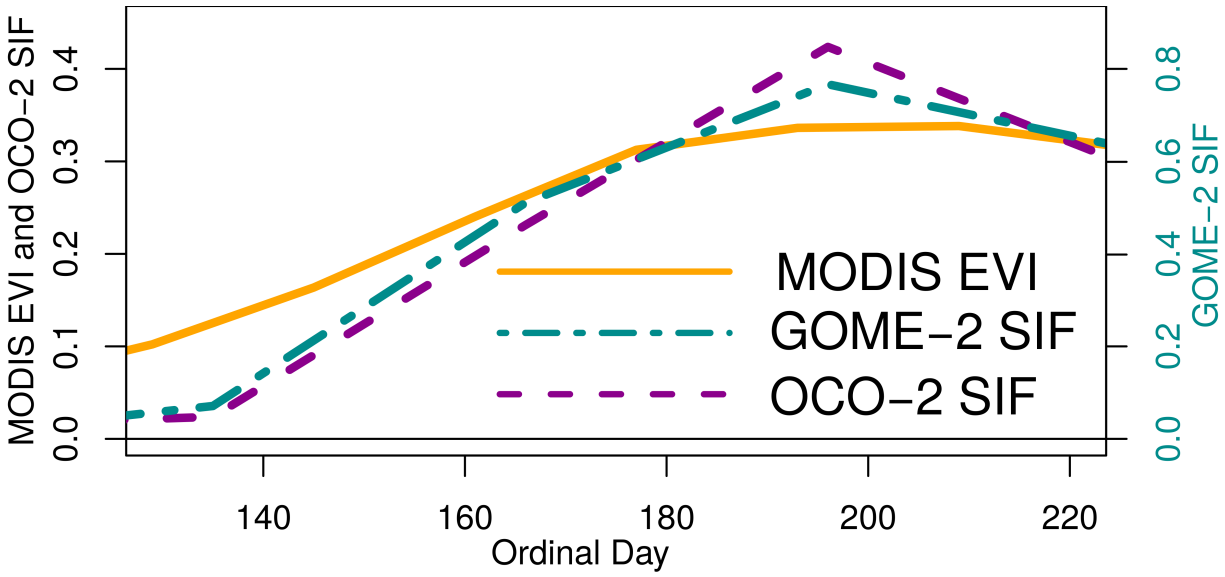

Figure 1. Spatially averaged 2014 seasonal cycle of MODIS EVI, OCO-2 SIF/cos(solar zenith angle) and GOME-2 SIF/cos(SZA) across Alaskan tundra.

Site	Latitude (° N)	Longitude (° W)	Vegetation	Ref.
Atqasuk	70.470	157.409	Moist-wet sedge	*Kwon et al.* [2006]
Barrow	71.323	156.626	Wet sedge tundra	*Lipson et al.* [2012]
Bonanza	64.701	148.321	Thermokarst bog	*Euskirchen et al.* [2014]
Imnavait	68.606	149.304	Wet tussock/sedge tundra	*Euskirchen et al.* [2012]

Table 1. Eddy covariance site descriptions

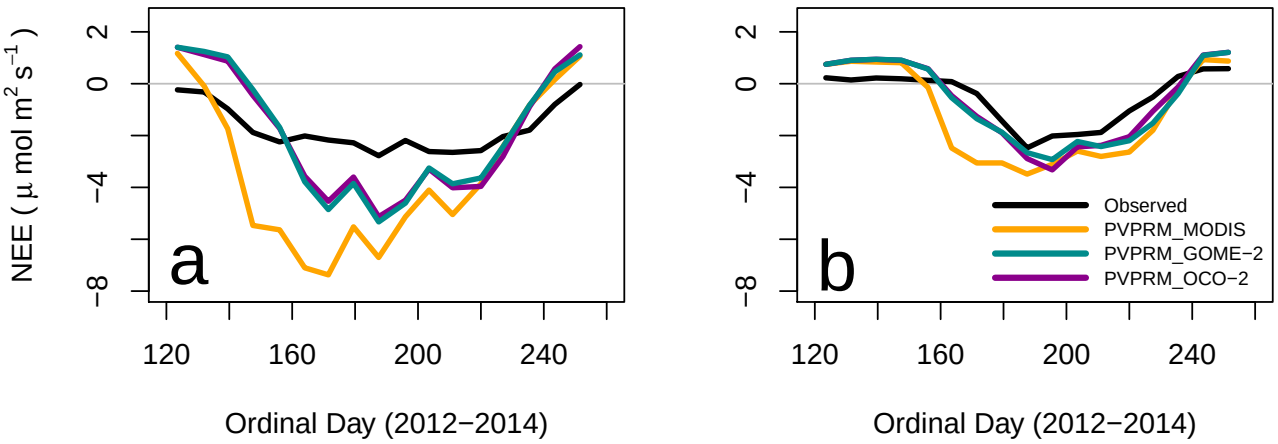

Figure 2. Time series (2012–2014) of mean eddy covariance NEE, EVI-based NEE, and SIF-based NEE at the Bonanza Creek thermokarst bog (a) and Imnavait wet sedge (b) sites, described in Table 1.

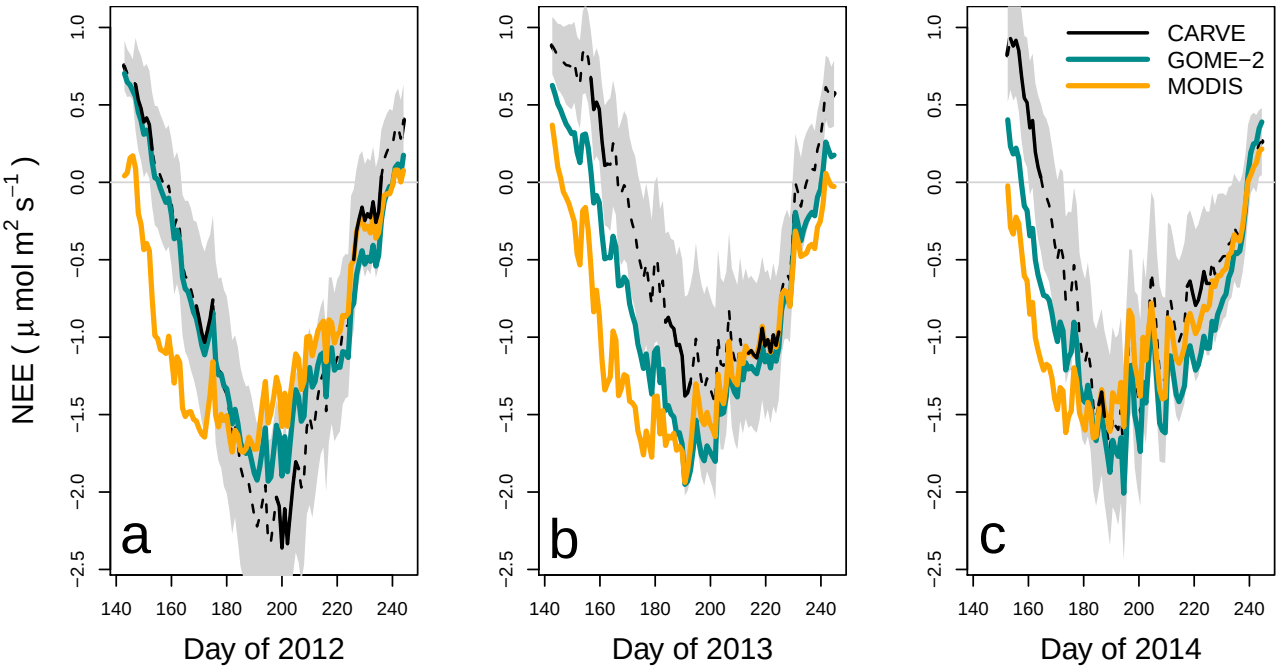

Figure 3. Spatially averaged Alaskan tundra NEE simulated using MODIS EVI and GOME-2 SIF, and CARVE-optimized NEE across Alaskan tundra in 2012 (a), 2013 (b) and 2014 (c). In all plots, the time series of mean CARVE-optimized NEE from 273 column profiles is indicated with a solid black line, interpolated NEE is indicated with a dotted line, and the standard deviation of the additive flux from CARVE column profiles is indicated in grey.

Table 2. Parameter values for all models (MODIS EVI, GOME-2 SIF and OCO-2 SIF). $T_{\min}$=0∘C and $T_{\max}$=40∘C for all models and vegetation classes [Figure S4].

Param	Model	Evgrn. Forest	Decid. Forest	Mixed Forest	Shrubs	Shrub Tundra	Graminoid Tun.	Wetland
λ	MODIS	0.234	0.127	0.123	0.122	0.040	0.030	0.149
λ	GOME-2	0.065	0.040	0.035	0.038	0.020	0.014	0.072
λ	OCO-2	0.117	0.061	0.064	0.064	0.046	0.028	0.160
PAR_0	All	262	570	629	321	241	241	241
T_{opt}	All	20	20	20	20	15	15	10